

## Reconciling temperature-dependent factors affecting mass transport losses in polymer electrolyte membrane electrolyzers

ChungHyuk Lee<sup>1</sup>, Jason K. Lee<sup>1</sup>, Michael G. George<sup>1</sup>, Kieran F. Fahy<sup>1</sup>, Jacob M. LaManna<sup>2</sup>, Elias Baltic<sup>2</sup>, Daniel S. Hussey<sup>2</sup>, David L. Jacobson<sup>2</sup>, Aimy Bazylak<sup>1,\*</sup>

<sup>1</sup>Thermofluids for Energy and Advanced Materials (TEAM) Laboratory  
Department of Mechanical and Industrial Engineering,  
University of Toronto Institute for Sustainable Energy  
Faculty of Applied Science and Engineering,  
University of Toronto, Toronto Ontario, Canada M5S 3G8

<sup>2</sup>Physical Measurement Laboratory, National Institute of Standards and Technology,  
Gaithersburg, Maryland, USA

### Abstract:

In this work, we investigated the impact of temperature on two-phase transport in low temperature (LT)-polymer electrolyte membrane (PEM) electrolyzer anode flow channels via *in operando* neutron imaging and observed a decrease in mass transport overpotential with increasing temperature. We observed an increase in anode oxygen gas content with increasing temperature, which was counter-intuitive to the trends in mass transport overpotential. We attributed this counterintuitive decrease in mass transport overpotential to the enhanced reactant distribution in the flow channels as a result of the temperature increase, determined via a one-dimensional analytical model. We further determined that gas accumulation and fluid property changes are competing, temperature-dependent contributors to mass transport overpotential; however, liquid water viscosity changes led to the dominate enhancement of reactant water distributions in the anode. We present this temperature-dependent mass transport overpotential as a great opportunity for further increasing the voltage efficiency of PEM electrolyzers.

**Keywords:** polymer electrolyte membrane electrolyzer; mass transport; anode flow channels; two-phase pressure drop; operating temperature; hydrogen

**\*Corresponding author:**

A. Bazylak

Mechanical & Industrial Engineering, Faculty of Applied Science & Engineering

University of Toronto

5 King's College Road Toronto, ON M5S 3G8

Tel: (416) 946-5031 Fax: (416) 978-7753 Email: [abazylak@mie.utoronto.ca](mailto:abazylak@mie.utoronto.ca)

## 1.0 Introduction

Hydrogen is an attractive energy vector that can enable the decarbonization of the current energy infrastructure [1]. Today, hydrogen is mainly produced by natural gas reforming, which heavily involves carbon emissions [2]. Electrochemical water-splitting via polymer electrolyte membrane (PEM) electrolysis is particularly promising means to produce hydrogen from intermittent renewable sources (such as solar panels [3]), and is projected to be the main electrolysis technology by 2030 [4]. The low temperature (LT)-PEM electrolyzer is attractive due to its rapid system response, compact design, and ability to operate over a wide range of current densities [5]. LT-PEM electrolyzer technologies have experienced rapid development over the last decade [6]; however, cost reduction remains paramount for widespread adoption [7]. To realize a cost-effective PEM electrolyzer system, important developments have been made on enhanced catalyst materials with improved catalytic activity [8] and alternative materials (i.e. catalyst [9] and flow field [10,11]) for cheaper electrolyzer components. Another exciting development to this end has been the linkage of increasing the PEM electrolyzer operating temperature with reduced power consumption, where the reduced power consumption has been attributed to decreases in kinetic overpotential, membrane resistance, and reversible potential [7]. However, higher operating temperatures ( $> 70$  °C) remain challenging to achieve in practice due to Nafion<sup>1</sup> membrane temperature sensitivity, instability of ion-exchange resins, poor catalyst durability, and unknown effects of multiphase flows in the anode (such as presence of gas bubbles and non-uniform liquid water distributions) [7,12].

---

<sup>1</sup> Certain trade names and company products are mentioned in the text or identified in an illustration in order to adequately specify the experimental procedure and equipment used. In no case does such identification imply recommendation or endorsement by the National Institute of Standards and Technology, nor does it imply that the products are necessarily the best available for the purpose.

Oxygen gas generation in the anode has a strong influence on the efficiency of PEM electrolyzers (via mass transport overpotentials) due to the oxygen gas displacement of reactant liquid water [13]. Oxygen must be continuously removed from the reaction sites for uninterrupted water delivery to the reaction sites. Suermann et al. [14] experimentally determined that the mass transport overpotential of their electrolyzer contributed up to 25 % of the total overpotential at current densities above 1 A/cm<sup>2</sup> for an operating pressure range between 1 bar to 100 bar. This overpotential was recently identified to be significantly affected by the proton transport resistance in the anode catalyst ionomer [15], as well as gas crossover across the membrane [16]. Furthermore, Li et al. [17] reported that their cell potential increased exponentially when they increased their operating temperature from 80 °C to 120 °C under atmospheric pressure operation. They attributed this exponential voltage growth to the rapid increase in mass transport overpotential caused by gaseous oxygen hindering the delivery of liquid water to the reaction sites. Several works [14,17-20] have identified the significance of anodic two-phase flow on PEM electrolyzer performance; however, the specific impact of operating temperature on the nature of two-phase flow remains relatively unexplored. In light of the insight from literature pointing to favourable higher temperature operation [7,12], understanding the impact of operating temperature on multi-phase transport phenomena in PEM electrolyzers is vital for tailoring operating conditions for this higher temperature operation. We hypothesize that the operating temperature has the potential to significantly affect mass transport overpotential via two-phase flow behaviour, due to the inherent dependence of fluid properties (i.e. viscosity, density, solubility, surface tension, and vapor pressure of water) on temperature.

While some researchers have found a correlation between higher operating temperature and reduced mass transport overpotential [21,22], there is an interesting discrepancy within the literature. Specifically, Ojong et al. [21] reported an increase in mass transport overpotential with increasing temperature, due to increasing reaction site blockage by oxygen gas with increasing temperature. On the other hand, Suermann et al. [22] reported a decrease in mass transport overpotential with increasing temperature, due to the temperature dependent changes in fluid properties (such as decreasing water viscosity and surface tension) that are favorable for water transport.. The works of Ojong et al. [21] and Suermann et al. [22] pose a duality in temperature effects that necessitate a closer examination of the effect of temperature on multi-phase transport and the directly-related mass transport overpotential in the PEM electrolyzer. Increasing the PEM electrolyzer operating temperature may encourage gas phase oxygen coverage that obstructs liquid water transport, but this increasing temperature may also enhance liquid water delivery due to favourable temperature-dependent variations in fluid properties. However, the relative contributions of these two mechanisms on the mass transport overpotential remain unclear, and this is a particularly pressing issue due to the nature of their opposing favourability on PEM electrolyzer efficiency. Although the temperature-dependence of mass transport overpotential has been demonstrated in previous works [21,22], an investigation of temperature-dependent mass transport overpotential using in operando imaging of the anode flow channels has not yet been reported in the literature.

The two-phase flow phenomenon in the anode flow field is a direct indicator of mass transport in PEM electrolyzers, as reported by previous works [23-27]. Dedigama et al. [25] and Ito et al. [24] have shown that the two-phase flow regime in the channel (i.e. slug or annular flow)

strongly influenced the resulting mass transport overpotential. Majasan et al. [28] have shown that parallel flow channels are superior relative to serpentine flow channels since serpentine flow channels promote the undesired slug flow in the flow channels and the subsequent increase in mass transport overpotential. Li et al. [29] have observed through thermal imaging that the temperature field in the flow channel is not uniform, where high local temperature was accompanied by higher gas generation rates. More recently, Zinser et al. [30] have reported that sufficient liquid water in the anode flow channels is a key driver for preventing drying-out at the anode catalyst layer. These results demonstrate the inherent link between the two-phase flow within the flow channel and the porous transport layer, as well as the catalyst layer. Although temperature effects on the two-phase flow near the PTL-CL interface have been investigated via neutron imaging in our previous work [31], the temperature effects on the two-phase flow within the anode flow channel also requires attention to achieve a fully-coupled understanding of temperature-dependent two-phase flow in PEM electrolyzers.

Since transparent materials do not exhibit the thermal and surface properties of the metallic flow fields used in practice, avoiding unrepresentative dynamic two-phase transport behaviour poses non-trivial challenges. Alternately, radiographic visualization is a promising means to study multiphase flow phenomena in an operating PEM electrolyzer [32-41]. X-ray synchrotron radiography offers in operando imaging with high spatial and temporal resolution, making the technique favorable for studying the dynamic behaviour of bubbles in PEM electrolyzers [35]. Leonard et al. [35] used X-ray imaging to investigate the oxygen bubble formation and detachment in an operating electrolyzer. They observed a decrease in bubble residence time in the channels with increasing current density [35]. Neutron radiography is also an attractive tool

for studying oxygen gas behaviour in PEM electrolyzers, due to the ability for neutrons to transmit through many metallic substances (compared to X-rays) [39]. Panchenko et al. [39] determined via neutron imaging that the stoichiometric ratio of liquid water in the anode flow channels should be greater than 100 to prevent congestion in oxygen gas transport and the subsequent increase in mass transport overpotential. Thanks to these pioneering studies, we now have a better understanding of the two-phase flow behavior within anode flow channels. These two-phase flow behaviors, however, are expected to be temperature-dependent, and a discussion of this temperature dependence is lacking in the body of literature. The urgent need of using imaging techniques to understand the temperature-dependent two-phase flow in PEM electrolyzers has been highlighted in the literature [22]. To the authors' best knowledge, investigations of the impact of temperature on multiphase transport in the flow channel and mass transport overpotential via *in operando* neutron imaging has not been reported in the literature.

In this work, we investigated the impact of operating temperature on the multiphase flow behaviour in the LT-PEM electrolyzer anode flow channels using *in operando* neutron radiography to explain the duality of temperature effects on mass transport overpotential. We simultaneously captured the electrochemical performance and the visualization data, allowing characterization of the relationship between the gas distribution across the anode flow channels and the mass transport overpotential. Specifically, we quantified the evolution of the anode gas thickness in the flow channels at three operating temperatures (40 °C, 60 °C, and 80 °C) to identify the influence of temperature on mass transport overpotential. Furthermore, we coupled the imaging results with an analytical model to elucidate the mechanistic cause of mass transport overpotential-dependence on temperature. Additionally, to isolate and identify the dominating

fluid property for affecting two-phase flow as a function of temperature, we predicted the two-phase pressure drop across the anode flow channels. Findings from this study reconcile the conflicting explanations of the effect of temperature on LT-PEM electrolyzers in the literature and suggest optimal operating conditions for enhanced performance of the electrolyzer.

## 2.0 Methodology

### 2.1 Electrolyzer cell assembly and testing setup

A custom, single-cell PEM electrolyzer was designed for *in operando* through-plane (neutron beam perpendicular to the active area) imaging. The active area of the cell was 80 mm<sup>2</sup> (5 mm in the direction of the reactant flow). The titanium flow field featured eight parallel channels separated by 1 mm wide ribs and the channels had a square cross-section with 1 mm sides. The flow field was plated with 0.5 μm thick gold and 2.5 μm thick platinum to avoid the formation of a passive oxide layer. The operating temperature of the electrolyzer was controlled by a water circulation bath (Isotemp heated bath circulator, Fisher Scientific). In the electrolyzer, the water circulation channels were located in close proximity to the membrane electrode assembly (MEA) for precise temperature control. A commercial catalyst coated Nafion 1110 membrane with a cathode platinum areal density of 0.3 mg/cm<sup>2</sup> and an anode iridium areal density of 1.0 mg/cm<sup>2</sup> (HYDRion N1110, Ion Power) were used, and a commercial 190 μm thick carbon paper (TGP-H-060, Toray Industries) was used as the cathode gas diffusion layer. A 300 μm thick sintered titanium powder porous transport layer (PTL) with a porosity of 54 % was used. The anode porous transport layer and the cathode gas diffusion layer thicknesses were controlled during assembly using polytetrafluoroethylene (PTFE) gaskets with thicknesses of 229 μm and 178 μm,

respectively. Specifically, the anode PTFE gasket was prescribed a thickness that was 24 % less than the anode PTL to ensure sufficient good electrical contact at the anode. To ensure the membrane-electrode assembly does not become over-compressed, a thick membrane was used and the cathode PTFE gasket was prescribed to be 6 % thinner than the cathode gas diffusion layer.

Deionized water was supplied to the anode compartment, and the flow rate was maintained at 20 mL/min via a peristaltic pump (Masterflex L/S precision variable-speed console drive, Cole-Parmer). The deionized water had a resistivity of 18 M $\Omega$ ·cm, and was not recirculated. A pulse dampener was placed in-line downstream of the peristaltic pump to supply stabilized reactant flow to the electrolyzer. The reactant water was heated through an in-line heater (Watlow fluent inline heater 500 W, Zesta Engineering LTD.) prior to entering the electrolyzer cell. The temperature of the water was monitored using an in-line thermocouple (Type K thermocouple, Zesta Engineering LTD.), and the output power of the heater was controlled using a PID temperature controller (Zesta benchtop PID control & limit, Zesta Engineering LTD.). Nitrogen gas was supplied to the cathode (*dry-cathode mode*) to maintain a dry cathode compartment. We intentionally suppressed changes in cathodic liquid water content in order to ensure dynamic changes in our visualizations could be attributed to mass transport in the anode compartment. In a previous study, we determined that a cathode purge rate of 10 L/min N<sub>2</sub> was sufficient for preventing liquid water accumulation in the cathode compartment [38]. The nitrogen purge rate was controlled by using a mass flow controller, and the tubing to the cathode compartment was heated to ensure that the purge gas temperature was maintained at the cell operating temperature. Direct current (DC) was supplied to the electrolyzer through a power supply (Genesys 750 W,

TDK-Lambda), and a potentiostat (IM6, Zahner) was used in potentiostatic mode to measure the high frequency resistance (HFR) of an operating cell with a frequency of 10 kHz.

The electrolyzer cell was operated at 40 °C, 60 °C, and 80 °C. The operating temperatures were held below the saturation temperature (i.e. 100 °C) to mitigate the effects of water evaporation on the mass transport overpotential. The cell temperature was monitored using a thermocouple placed in the anode flow field, located 5 mm away from the active area. At each operating temperature, the electrolyzer was tested at three current densities, 1.0 A/cm<sup>2</sup>, 2.0 A/cm<sup>2</sup>, and 3.0 A/cm<sup>2</sup> (held for 20 minutes each). Although these current densities were not sufficiently high for mass transport overpotentials to dominate, we applied operating conditions that are commercially relevant ( $i \leq 3$  A/cm<sup>2</sup> [6] and large water flow rates for cooling [24]) to investigate the significance of mass transport effects under commercially relevant conditions. During the last five minutes of each constant current operation, the HFR of the electrolyzer was measured at 10 kHz. The cell potential was recorded using a custom test station at a rate of 1 point/second.

## 2.2 Mass transport overpotential calculation

Mass transport overpotential was calculated using the following relation:

$$\eta_{\text{mass transport}} = E_{\text{cell}} - E_{\text{reversible}} - \eta_{\text{ohmic}} - \eta_{\text{kinetic}} \quad (1)$$

where  $\eta_{\text{mass transport}}$  is the mass transport overpotential [V],  $E_{\text{cell}}$  is the measured cell potential [V],  $E_{\text{reversible}}$  is the reversible potential [V],  $\eta_{\text{ohmic}}$  is the ohmic overpotential [V], and  $\eta_{\text{kinetic}}$

is the kinetic overpotential [V]. The reversible potential was estimated using the expression reported by LeRoy et al. [42] for water electrolysis:

$$E_{\text{reversible}} = 1.5184 - 1.5421 \times 10^{-3} \cdot T + 9.523 \times 10^{-5} \cdot T \cdot \ln T + 9.84 \times 10^{-8} \cdot T^2 \quad (2)$$

where  $T$  is the operating temperature [K]. The ohmic overpotential in Equation (1),  $\eta_{\text{ohmic}}$ , was determined based on the current density and measured ohmic resistance using Ohm's law:

$$\eta_{\text{ohmic}} = i \cdot R_{\text{ohmic}} \quad (3)$$

where  $i$  is the current density [ $\text{A}/\text{cm}^2$ ], and  $R_{\text{ohmic}}$  is the measured HFR [ $\Omega \cdot \text{cm}^2$ ]. The internal resistance (IR)-corrected cell potential was obtained by subtracting the ohmic overpotential from the measured cell potential. Suermann et al. [22] reported an IR-corrected cell potential with a linear behaviour at low current densities, where a fit to the Tafel line describes the kinetic overpotential as follows:

$$\eta_{\text{kinetic}} = b \cdot \log_{10}\left(\frac{i}{i_0}\right) \quad (4)$$

where  $b$  is the Tafel slope [V/dec], and  $i_0$  is the apparent exchange current density [ $\text{A}/\text{cm}^2$ ]. In this work, the exchange current density and the Tafel slope were based on Tafel region measurements. For determining the Tafel region measurements, we varied the current density from  $5 \text{ mA}/\text{cm}^2$  to  $300 \text{ mA}/\text{cm}^2$ , which was automated and supplied by a potentiostat (VersaSTAT 3, Princeton Applied Research, Oak Ridge, TN).

We quantified the voltage efficiency of the electrolyzer to further elucidate the contribution of temperature-dependent overpotentials on the cell performance. The voltage efficiency was defined as follows:

$$\eta_v = \frac{E_{rev}}{E_{cell}} \times 100 \% \quad (5)$$

where  $\eta_v$  denotes the voltage efficiency of the cell [%].

### *2.3 Neutron radiographic imaging and processing*

*In operando* neutron imaging of the operating electrolyzer cell was performed at the Neutron Imaging Facility (BT-2) at the National Institute of Standards and Technology (NIST) in Gaithersburg, Maryland. The electrolyzer cell was oriented in the through-plane direction of the neutron beam, as shown in Fig. 1a. Specifically, the anode flow channels were imaged to elucidate the temperature-dependent two-phase flow behavior in the anode flow channels. The elucidated two-phase flow behavior allowed us to reconcile the duality of temperature effects on mass transport in the electrolyzer (i.e. effects of change in temperature-dependent fluid properties) and subsequently couple the temperature effects on mass transport with the mass transport overpotential determined from the analysis presented in Section 2.2. Neutron beams transmitted through the electrolyzer cell were absorbed and converted into visible light by the  $\text{Gd}_2\text{O}_2\text{S:Tb}$  scintillator. An Andor Neo scientific complementary metal-oxide semiconductor (sCMOS) sensor was used to detect the visible light emitted by the scintillator. The exposure time of each image was 60 seconds, and the pixel pitch was  $6.5 \mu\text{m}$  for a resolution of  $\sim 20 \mu\text{m}$ . A radiographic reference image was obtained when the anode compartment was fully filled with liquid water, the cathode compartment was dry, and power was not supplied to the electrolyzer cell. Our cell included a total of eight channels, and the centrally positioned six channels were visualized (Channels 2-7, see Fig. 1b).

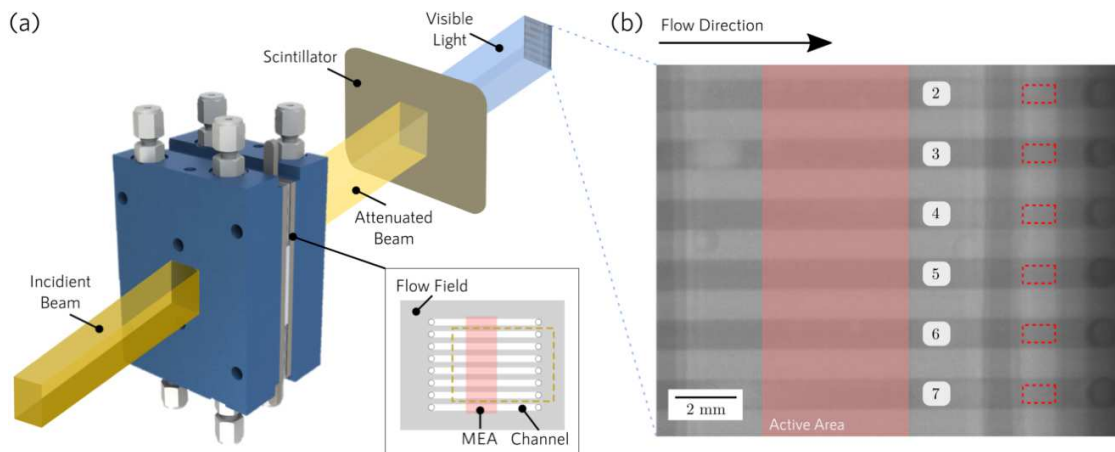


Figure 1: (a) A schematic of the neutron imaging setup: incident beam originating from a nuclear reactor traverses in the through-plane direction (beam perpendicular to the membrane). The attenuated beam meets the scintillator, and the scintillator emits visible light based on the intensity of the attenuated beam. The inset schematic (black-solid box) shows the geometry of the flow field and the membrane-electrode-assembly (MEA). The yellow-dashed box indicates the imaged region. (b) Processed image of the electrolyzer. The position of the active area is indicated by the shaded red region, and channels are numbered as shown. Gas thicknesses were quantified for the regions dashed in red.

All of the obtained images were processed in the following sequence: (1) median combination of three images, (2) median filtering 3-by-3 pixels, (3) combined wavelet-Fourier filtering [43], (4) image registration [44], and (5) application of the Beer-Lambert law. The median combination step was used to remove gamma spots from the images. Gamma spots are noise artefacts that are spatially inconsistent among all images and originate from high energy photons generated as a by-product of neutron imaging. The median filtering step was used to eliminate hot spots, which were noise artefacts caused by the hardware (such as sCMOS) used in the experimental setup. A combined wavelet-Fourier filtering tool [43] was used to separate and eliminate the stripe-like artefacts from the original image. An image registration process [44] was used to account for the fluctuation of the beam source at the BT-2 beamline which otherwise caused a change in the intensity profile of the beam relative to the electrolyzer cell. Finally, the changes in intensity between the reference images and the operational images were quantified with the Beer-Lambert

law. The calibrated Beer-Lambert law reported by Hussey et al. [44] was used to quantify the gas thickness in the anode flow channels as follows:

$$t_{\text{gas}} = \sqrt{-\frac{\ln(I/I_0)}{\beta_w} + \frac{\Sigma_w^2}{4\beta_w^2}} - \frac{\Sigma_w}{2\beta_w} \quad (6)$$

where  $t_{\text{gas}}$  is gas thickness [mm], herein termed *gas thickness*. In Equation (6),  $I$  is the pixel intensity from the operational images;  $I_0$  is the pixel intensity from the reference image;  $\beta_w$  [ $-0.00947 \text{ mm}^{-2}$ ] and  $\Sigma_w$  [ $0.38483 \text{ mm}^{-1}$ ] are the calibration coefficients for water obtained from non-linear least square fitting [44]. A sample of a resulting processed image (prior to applying the Beer-Lambert law) is shown in Fig. 1b. The image shown in Fig. 1b is an average of 9 images (i.e. 9 minutes) and the 9 images were captured after 10 minutes of operation at each constant current step. The exit gas thicknesses were in the regions highlighted by red-dashed boxes in Fig 1b (outside of the active area). By selecting regions outside of the active area, we directly correlated the pixel intensity to the presence of oxygen gas in the anode flow channels (where possible dynamics in the catalyst layer and membrane did not play a role).

#### 2.4 Two-phase flow modelling to examine uniformity of liquid water distribution

Here, we present a one-dimensional (1D) analytical model for calculating the oxygen gas thickness at the exit of the anode flow channel with the assumption that the reactant liquid water is uniformly distributed along the channel. We hypothesized that the operating temperature can significantly influence the degree of liquid water distribution in the anode flow channels. During neutron imaging, the gas thickness was measured over a period of 60 seconds (exposure time) for each image, but the velocities of bubble and liquid water within each channel were not resolved.

Hence, an analytical model was developed to compare the gas thicknesses determined experimentally and analytically to examine the liquid water distributions expected in our experiments. The computational domain is illustrated in Fig. 2.

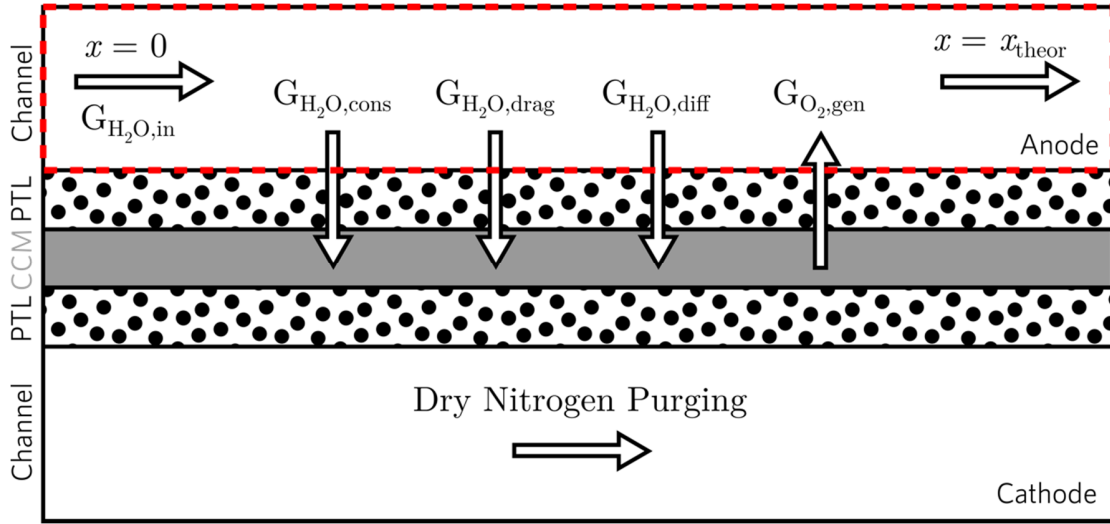


Figure 2: Schematic outlining the parameters considered in the 1D analytical model to solve for theoretical gas thickness in the channels. This theoretical gas thickness assumes uniform reactant distribution and operating current density across the active area. Each term of the model is summarized in Table 1. The red-dashed box indicates the anode flow channel, which is the region of interest for the calculation.

Following the procedure reported by Ito et al. [24], the mass flow ratio of gas and water (or quality) of the two-phase flow in the anode channels,  $x_{theor}$ , was estimated using the following equation:

$$x_{theor} = \frac{G_{O_2,gen}}{G_{H_2O,in} - G_{H_2O,cons} - G_{H_2O,drag} - G_{H_2O,diff} + G_{O_2,gen}} \quad (7)$$

where  $G_{O_2,gen}$  is the theoretical oxygen mass generation flux [ $kg/(m^2 \cdot s)$ ],  $G_{H_2O,in}$  is the supplied water mass flux [ $kg/(m^2 \cdot s)$ ],  $G_{H_2O,cons}$  is the theoretical water consumption mass flux due to the oxygen evolution reaction [ $kg/(m^2 \cdot s)$ ], and  $G_{H_2O,drag}$  and  $G_{H_2O,diff}$  are the theoretical water

crossover mass fluxes due to electro-osmotic drag and diffusion, respectively [kg/(m<sup>2</sup>·s)]. The details of each term are listed in Table 1.

Table 1: Equations for the mass flux terms in Equation (7) [24]

Mass Flux Term	Equation
$G_{O_2,gen}$	$\frac{i \cdot A_{cell} \cdot M_{O_2}}{4 \cdot F \cdot n \cdot A_{channel}}$
$G_{H_2O,in}$	$\frac{Q_{H_2O} \cdot \rho_{H_2O}}{n \cdot A_{channel}}$
$G_{H_2O,cons}$	$\frac{i \cdot A_{cell} \cdot M_{H_2O}}{2 \cdot F \cdot n \cdot A_{channel}}$
$G_{H_2O,drag}$	$(0.0134 \times T + 0.03) \frac{i \cdot A_{cell} \cdot M_{H_2O}}{F \cdot n \cdot A_{channel}}$

In this work, we also considered the mass flux due to diffusion,  $G_{H_2O,diff}$  in Equation (7), due to the dry-state of the cathode compartment (due to dry-cathode mode operation, see Fig. 2). The mass flux due to diffusion was defined using Fick's law:

$$G_{H_2O,diff} = M_{H_2O} \cdot D_w \cdot \frac{\rho_{mem}}{M_{mem}} \cdot \frac{(\lambda_{anode} - \lambda_{cathode})}{t_{mem} \cdot a_{mem}} \cdot \frac{A_{cell}}{n \cdot A_{channel}} \quad (8)$$

where  $M_{H_2O}$  is the molecular weight of water [0.018 kg/mol],  $D_w$  is the Fickian diffusion coefficient of water across the membrane [m<sup>2</sup>/s],  $\rho_{mem}$  is the density of the membrane [1980 kg/m<sup>3</sup>],  $M_{mem}$  is the molecular weight of the membrane [1.1 kg/mol],  $\lambda_{anode}$  and  $\lambda_{cathode}$  are water contents (mol water per mol sulfonic acid) of the anode and cathode side of the membrane, respectively,  $t_{mem}$  is the membrane thickness [ $2.5 \times 10^{-4}$  m],  $a_{mem}$  is the membrane activity,  $A_{cell}$  is the active area [ $8.0 \times 10^{-7}$  m<sup>2</sup>],  $n$  is the number of channels, and  $A_{channel}$  is the cross-sectional area of each channel [ $1.0 \times 10^{-6}$  m<sup>2</sup>]. The diffusion coefficient,  $D_w$  in Equation

(8) was estimated based on the correlation reported by Motupally et al. [45] for liquid water transport through Nafion membranes:

$$\begin{cases} D_w = 3.10 \times 10^{-7} \cdot \lambda_{mem} \cdot [-1 + e^{(0.28\lambda_{mem})}] \cdot e^{\frac{-2436}{T}} & \lambda_{mem} \leq 3 \\ D_w = 4.17 \times 10^{-8} \cdot \lambda_{mem} \cdot [1 + 161e^{(-\lambda_{mem})}] \cdot e^{\frac{-2436}{T}} & \lambda_{mem} > 3 \end{cases} \quad (9)$$

where  $\lambda_{mem}$  is the water content of the membrane and was assumed to be an average of  $\lambda_{anode}$ , and  $\lambda_{cathode}$ . The  $D_w$  values in this work were assumed to be  $1.92 \times 10^{-10}$  m<sup>2</sup>/s,  $3.07 \times 10^{-10}$  m<sup>2</sup>/s,  $4.64 \times 10^{-10}$  m<sup>2</sup>/s for 40 °C, 60 °C, and 80 °C, respectively. A value of 22 was assumed for  $\lambda_{anode}$  since the water uptake of a liquid water-equilibrated Nafion membrane has been shown to be 22 [45], and the anode was constantly supplied with liquid water in our study.  $\lambda_{cathode}$  was assumed to be zero, because the cathode was constantly purged with dry nitrogen. A sensitivity analysis was performed to examine the sensitivity of the model to this assumption, and the results are reported in the Appendix. Also, the activity of the membrane ( $a_{mem}$ ) was assumed to be 1, since the membrane was in contact with liquid water on the anode side.

The theoretical gas thickness ( $t_{O_2,theor}$ ) was calculated from the theoretical quality ( $x_{theor}$ ) using the following relation:

$$x_{theor} = \frac{t_{O_2,theor} \cdot \rho_{O_2} \cdot A}{t_{O_2,theor} \cdot \rho_{O_2} \cdot A + (t_{channel} - t_{O_2,theor}) \cdot \rho_{H_2O} \cdot A} \quad (10)$$

where  $\rho_{O_2}$  is the density of oxygen [kg/m<sup>3</sup>],  $A$  is the area of the considered region for quantifying the gas thickness [mm<sup>2</sup>],  $t_{channel}$  is the depth of the channel [mm], and  $\rho_{H_2O}$  is the density of liquid water [kg/mm<sup>3</sup>]. We modelled the theoretical gas thickness ( $t_{O_2,theor}$ ) for a

range of operating current densities ( $0 \text{ A/cm}^2 \leq i \leq 3 \text{ A/cm}^2$ ) and temperatures (40 °C, 60 °C, and 80 °C) to simulate our experimental conditions. Ultimately, we used this model to evaluate how applicable the uniform liquid water distribution assumption was for our experimental conditions.

### *2.5 Two-phase pressure drop calculation for determining dominating fluid property*

Previous researchers have reported various temperature-sensitive fluid properties that potentially affect mass transport overpotential in the electrolyzer (such as gas coverage in the electrode [21], gas density and surface tension [32], and water viscosity and wettability [22]); however, there is a lack of a consensus and any direct evidence linking these fluid properties to temperature-dependent mass transport overpotential. Here, we outline our procedure for determining which fluid property dominates the two-phase flow behaviour in the electrolyzer by calculating the two-phase pressure drops across the flow channels. The two-phase pressure drop in flow channels has been validated as a diagnostic tool for mass transport losses in PEM fuel cell systems [46]. The pressure drop across the anode flow field is a key indicator for mass transport in PEM electrolyzers since permeation is one of the main mechanisms of liquid water transport [47]. We performed a fluid-property based sensitivity analysis to identify the property that drives the change in mass transport overpotential with increasing temperature. The two-phase pressure drop over a channel length was determined as follows:

$$\Delta P_{\text{TP}} = \frac{\Delta P_{\text{LO}}}{L} \int_0^L (1 - x) \cdot \phi_L^2 dz \quad (11)$$

where  $\Delta P_{\text{TP}}$  is the two-phase pressure drop across a channel [Pa],  $\Delta P_{\text{LO}}$  is the single-phase (liquid only) pressure drop across a channel [Pa],  $L$  is the channel length [m], and  $\phi_L$  is the two-phase multiplier [-]. We used the Lockhart-Martinelli correlation [48] to determine the two-phase multiplier ( $\phi_L$ ), which is the fraction between the pressure drop with liquid-phase only.

$$\phi_L^2 = 1 + \frac{C}{X} + \frac{1}{X^2} \quad (12)$$

where  $C$  is the Chisholm parameter, and  $X$  is the Lockhart-Martinelli parameter. The Chisholm parameter is dependent on the superficial velocities of the liquid and the gas phase, and the Lockhart-Martinelli parameter is dependent on the density and the viscosity of each phase, as well as the quality. The correlation has been validated by Ito et al. [24] for quantifying two-phase pressure drop across PEM electrolyzer flow channels. The details on calculating each parameter are summarized in Table 2.

Table 2: Lockhart-Martinelli parameter (X) and Chisholm parameters (C) [24]

Flow Regime		Lockhart-Martinelli Parameter (X)	Chisholm Parameter (C)
Liquid	Gas		
Laminar	Turbulent	$\left(\frac{1-x}{x}\right)^{1/2} \left(\frac{\rho_g}{\rho_l}\right)^{1/2} \left(\frac{\mu_l}{\mu_g}\right)^{1/2}$	5
Turbulent	Laminar	$0.075 \cdot \text{Re}_{\text{H}_2\text{O}}^{0.375} \left(\frac{1-x}{x}\right)^{1/2} \left(\frac{\rho_g}{\rho_l}\right)^{1/2} \left(\frac{\mu_l}{\mu_g}\right)^{1/2}$	10
Laminar	Turbulent	$13.4 \cdot \text{Re}_{\text{O}_2}^{-0.375} \left(\frac{1-x}{x}\right)^{1/2} \left(\frac{\rho_g}{\rho_l}\right)^{1/2} \left(\frac{\mu_l}{\mu_g}\right)^{1/2}$	12
Turbulent	Turbulent	$\left(\frac{1-x}{x}\right)^{0.875} \left(\frac{\rho_g}{\rho_l}\right)^{1/2} \left(\frac{\mu_l}{\mu_g}\right)^{0.125}$	21

Using the equations listed in Table 2, the Lockhart-Martinelli parameter and the Chisholm parameter were determined by inputting the experimentally measured quality and known fluid properties. The fluid properties used for the calculations are listed in Table 3.

Table 3: List of fluid properties used for the quality calculations and the pressure-drop ratio calculation [49,50]

	Cell temperature, $T_{\text{cell}}$		
	40 °C	60 °C	80 °C
Viscosity of water ( $\times 10^{-4}$ ) [Pa·s]	6.53	4.66	3.54

Viscosity of oxygen ( $\times 10^{-5}$ ) [Pa·s]	2.13	2.24	2.34
Density of water [kg/m <sup>3</sup> ]	992	983	972
Density of oxygen [kg/m <sup>3</sup> ]	1.25	1.17	1.10

Pressure drop assuming single-phase ( $\Delta P_{LO}$ ) was calculated using the following equation:

$$\Delta P_{LO} = \frac{C_f}{t_{channel}} \cdot L \cdot \frac{G_{H_2O,in}^2}{\rho_{H_2O}} \quad (13)$$

where  $C_f$  is the friction coefficient based on the Reynolds number of the flowing liquid water [-].

A more in-depth calculation procedure is detailed in the Appendix. Liquid water was assumed to be uniformly distributed in each parallel channel, and the effects of gravity or compressibility were neglected in the calculation. Additionally, through sensitivity analyses of the two-phase pressure drop, we determined which fluid property that dominates the two-phase pressure drop.

### 3.0 Results & Discussion

We first discuss the experimentally determined ohmic, kinetic, and mass transport overpotentials for operating temperatures of 40 °C, 60 °C, and 80 °C and present the gas thicknesses in the anode flow channels measured via neutron imaging. We compare the imaging results with our theoretical calculations to evaluate the uniformity of liquid water distribution along the channel.

We then report the two-phase pressure drop calculated using the Lockhart-Martinelli correlations to identify which temperature-sensitive fluid property dominates the mass transport overpotential.

#### 3.1 Temperature Dependence of Overpotentials

The galvanostatic polarization curves for the electrolyzer demonstrated the relationship between increasing operating temperature and decreasing total overpotential (Fig. 3a). Specifically, while we observed a relatively constant ohmic resistance with increasing current density, we observed a notable decrease in ohmic resistance with increasing temperature (Fig. 3a). This decrease in ohmic resistance was attributed to the increased ionic conductivity of the membrane, which has been observed in previous works [51]. The change in electronic conductivity was assumed to be negligible, given the small thickness of the PTL and the relatively large thickness of the membrane. Furthermore, an identical cell assembly was used for all three operating temperatures, implying that a similar electronic resistance is expected. The ionic conductivity of the membrane was expected to increase with increasing temperature due to the changes in the activity of the membrane with increasing temperature [52]. Specifically, the independence of the ohmic resistance to the current density implies that the water content of the membrane did not significantly change with increasing current density, even though the cathode was actively dried. Koptizke et al. [52] measured an increase in ionic conductivity with increasing temperature when Nafion was submerged in liquid water, and they attributed this behaviour to the Arrhenius-type behavior of the Nafion membrane activity. These findings are also in agreement with the literature [51].

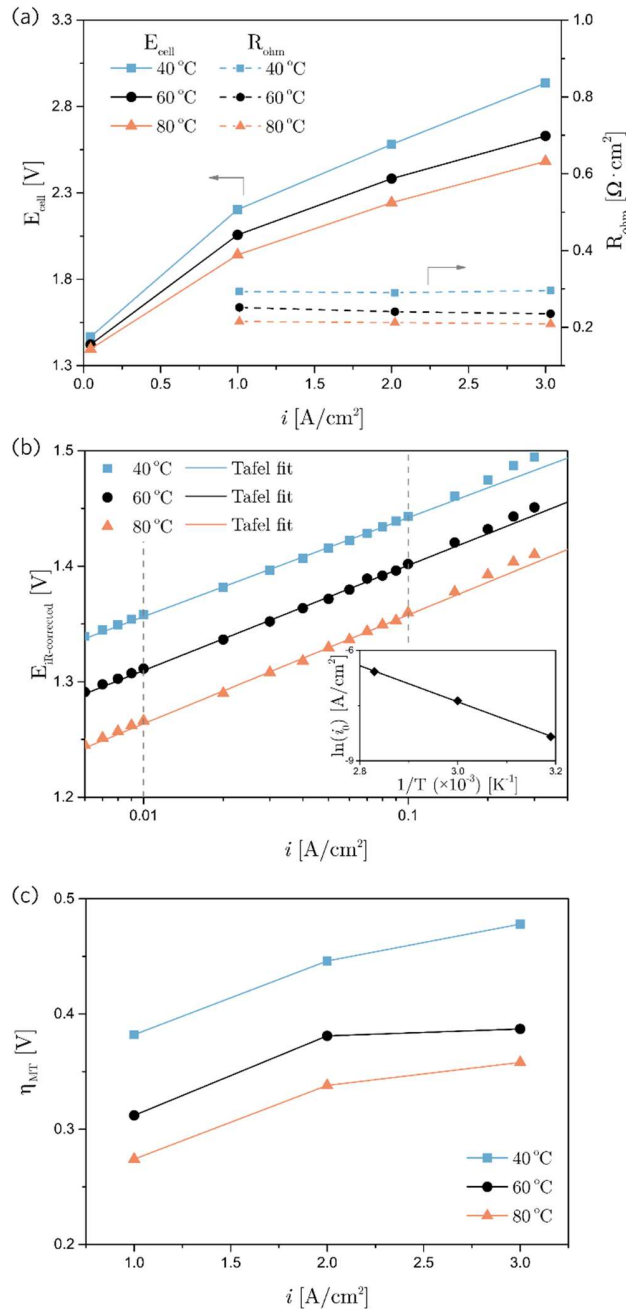


Figure 3: (a) Galvanostatic polarization curves and the ohmic resistances of the electrolyzer cell operated at 40 °C, 60 °C, and 80 °C. The decrease in ohmic resistance was a main contributor to the decrease in cell potential with increasing temperature in this experiment. We attributed a significant portion of this ohmic resistance decrease to the decreasing membrane resistance of the relatively thick membrane used (250  $\mu\text{m}$  thick) as a function of increasing temperature. (b) Tafel plots for determining the kinetic overpotential. The Tafel region was considered from 10  $\text{mA}/\text{cm}^2$  to 100  $\text{mA}/\text{cm}^2$ , indicated between dashed grey lines. This range was justified by the slight lift-off of the  $iR$ -corrected cell potential from the Tafel line when  $i > 0.1$   $\text{A}/\text{cm}^2$  and by the

demonstrated Arrhenius relation (inset of (b)). (c) The trend in mass transport overpotentials with increasing operating temperatures. We observed a decrease in mass transport overpotential with increasing temperature.

The kinetic overpotential in the operating cell was calculated from the IR-corrected cell potential in the Tafel region (Fig. 3b). In this work, the Tafel region was considered between current densities 10 mA/cm<sup>2</sup> to 100 mA/cm<sup>2</sup>, as suggested by Suermann et al. [22] The measurements were repeated three times and were repeatable with a variation of ±1.3 mV, ±2.2 mV, and ±1.7 mV in the iR-corrected potentials for 40 °C, 60 °C, and 80 °C, respectively. We observed a minor deviation of the IR-corrected cell potential from the extrapolated Tafel line for current densities greater than  $i = 100$  mA/cm<sup>2</sup>, thereby verifying the appropriateness of our current density range for determining the Tafel parameters. Specifically, the minor deviation from the Tafel line indicated the presence of a mass transport overpotential for current densities greater than  $i = 100$  mA/cm<sup>2</sup>, and for current densities below  $i = 100$  mA/cm<sup>2</sup>, the electrolyzer performance was dominated by kinetic overpotentials. Additionally, we observed an Arrhenius relationship between the operating temperature and the apparent exchange current densities (Fig. 3b inset), which further supports our Tafel parameter determination. We observed an increase in the apparent exchange current density (listed in Table 4), which indicates a decrease in kinetic overpotential with increasing temperature. Previously, the apparent exchange current density values were reported to be on the order of 10<sup>-6</sup> to 10<sup>-7</sup> [22]. The difference between the values reported in this work and in the literature may have been due to the large dry nitrogen purge rate at the cathode compartment. A previous work [22] showed the dependence of the apparent exchange current density on gas pressure, where a larger gas pressure led to an increase in the apparent exchange current density. The effect of operating temperature on the apparent exchange

current density was outside the scope of this study, but future work may be pursued to understand how a dry-cathode mode affects the apparent exchange current density. These parameters were used to quantify the kinetic overpotential under all operation conditions tested in this study.

Table 4: Measurement of parameters used for determining the kinetic overpotential.

Cell temperature, $T_{\text{cell}}$ [°C]	Tafel slope, $b$ ( $\times 10^{-2}$ ) [V/dec]	Exchange current density, $i_0$ ( $\times 10^{-4}$ ) [A/cm <sup>2</sup> ]
40	8.62	2.38
60	9.15	6.28
80	9.41	13.9

Based on the measured cell potential, ohmic resistance, Tafel slope, and the exchange current density, the mass transport overpotential was determined and presented in Fig. 3c. The mass transport overpotential decreased with increasing operating temperature. At 3.0 A/cm<sup>2</sup>, when the temperature increased from 40 °C to 80 °C, the mass transport overpotential decreased by 25 % (from 0.48 V to 0.36 V). The trends in the dependence of mass transport overpotential on temperature are in agreement with results reported by Suermann et al. [22] Previous works [15,53,54] that employed an identical calculation method have discovered factors that mainly influence the mass transport overpotential, such as (1) the current density-dependent gas crossover, (2) proton transport resistance within the anode CL ionomer, and (3) mass transport within the anode CL. We detailed here a discussion of each factor that may affect our experimental results, to hypothesize the mechanism of the decrease in mass transport overpotential with increasing temperature in our experiment.

(1) Current density-dependent gas crossover: In this discussion, we assumed a negligible gas crossover effect, since a relatively thick membrane (i.e. N1110) was used, and the cell was operated at atmospheric pressure.

(2) Proton transport resistance in the anode CL: This proton transport resistance has been shown to account for up to 21 % of the mass transport overpotential at 3 A/cm<sup>2</sup> [15], and could have played a significant role in the temperature-dependence of the mass transport overpotential. However, we observed up to a 19 % decrease in the overall mass transport overpotential when increasing the operating temperature from 40 °C to 60 °C, which is much greater than the reported temperature-dependence of proton transport resistance in the ionomer [15]. Specifically, an increase in the operating temperature from 50 °C to 70 °C resulted in a decrease in ionic resistance in the anode CL ionomer by 30 %, which would account for the 6 % decrease in the total mass transport overpotential (assuming that the contribution of the ionic transport resistance in the anode CL ionomer to the mass transport overpotential is 21 %).

(3) Mass transport within the CL: Mass transport in the CL has been shown to be a significant contributor to the mass transport overpotential [54,55]. Specifically, Schuler et al. [54] suggested that the liquid water transport from the PTL pores to the PTL/CL contact points via in-plane permeation of liquid water. As recently reported by Ziner et al. [30], the gas distribution in the PTL pores is significantly affected by the gas volume in the anode flow channels, which is expected to subsequently affect the liquid water transport within the catalyst layer.

We hypothesized that the decrease in the mass transport overpotential was mainly driven by the mass transport within the flow channel, the PTL, and the anode CL. Although the temperature-dependence of the gas accumulation in the anode CL and PTL interface has been recently reported [31], the temperature-dependent two-phase flow in the anode flow channel has not yet been reported in the literature.

It is also important to note that the mass transport overpotential reported in this work is relatively higher than the previously reported values [22]. We attribute the relatively higher overpotential to the following possible reasons: (1) the large flow field land widths relative to the active area may have caused non-uniform compression, and (2) low local flow rate of liquid water, which was employed to explore the limiting performance of the PEM electrolyzer. In this work, our focus was to fundamentally understand the effects of temperature on the mass transport overpotential by comparing relative the overpotential values determined via experiment. To be conservative, we did not draw any conclusions on the absolute values of the overpotentials, but rather we focused on the relative overpotential comparisons.

We further elucidate the contribution of mass transport losses to the cell performance by determining the voltage efficiency of the electrolyzer (Fig. 4a). A significant improvement in the voltage efficiency was observed, where we observed a 7 % increase in the voltage efficiency from  $T = 40\text{ }^{\circ}\text{C}$  to  $T = 80\text{ }^{\circ}\text{C}$  at  $i = 3.0\text{ A/cm}^2$ . This increase in voltage efficiency is attributed to decreases in kinetic, ohmic, and mass transport overpotentials, which were all strongly temperature-dependent (Fig. 4b). However, kinetic and ohmic overpotentials have been

extensively studied [21,22,56] and are closely associated with the materials used, such as the catalyst loading and the membrane thickness, respectively. On the other hand, the mechanistic cause of the mass transport overpotential, which contributed 28 % of the total overpotential (and > 20% throughout  $1 \text{ A/cm}^2 \leq i \leq 3 \text{ A/cm}^2$ ), remains relatively unknown, and presents a great opportunity for further increasing the voltage efficiency.

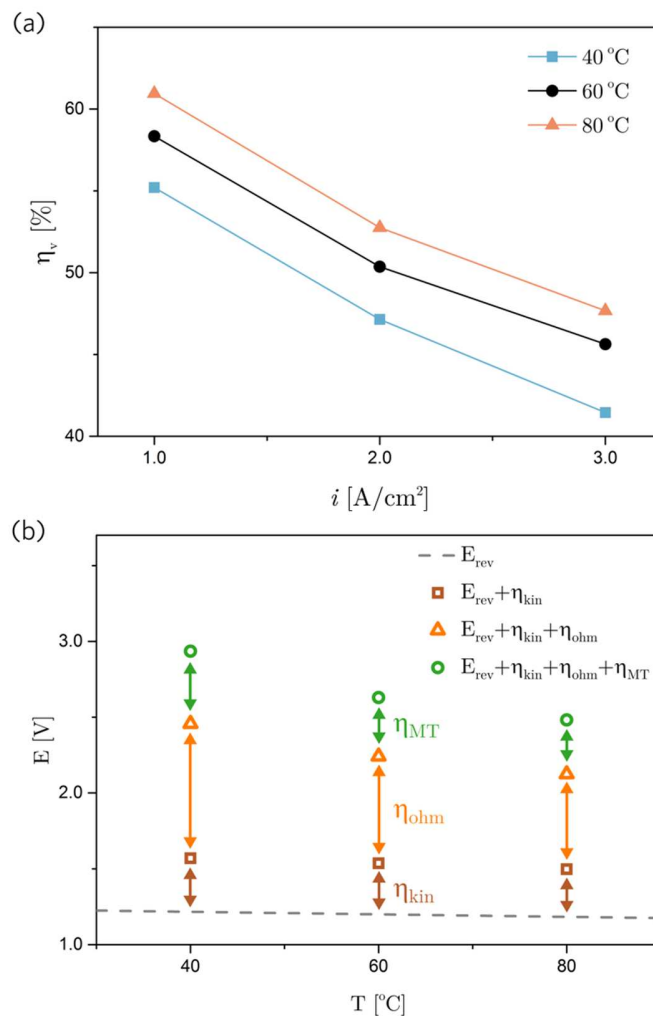


Figure 4: (a) Voltage efficiency of the electrolyzer as a function of operating temperature. At  $i = 3.0 \text{ A/cm}^2$ , we observed a 7 % increase in the voltage efficiency from  $T = 40 \text{ °C}$  to  $T = 80 \text{ °C}$ . (b) Breakdown of the overpotentials at  $i = 3.0 \text{ A/cm}^2$ . The dashed-line indicates the reversible potential, the brown, orange, and green arrows indicate kinetic, ohmic, and mass transport overpotential, respectively. Mass transport overpotential contributed up to 28 % of the total overpotential, which highlights a major opportunity for improving the voltage efficiency of the electrolyzer.

### *3.2 Higher Temperature Promotes Uniform Reactant Distribution*

The measured cumulative thickness of the gas phase in the beam path (herein referred to as *gas thickness*, or  $t_{\text{gas}}$ ) in each anode flow channel at an operating current density of  $3.0 \text{ A/cm}^2$  is presented in Fig. 5. The content of gas increased with increasing temperature for each channel, as shown in the neutron images (Fig. 5a-c) and corresponding gas thicknesses (Fig. 5d). The mean quantity of gas increased by 46 % (from 0.24 mm to 0.35 mm) when the operating temperature increased from  $40 \text{ }^\circ\text{C}$  to  $80 \text{ }^\circ\text{C}$ . Such a dramatic increase in gas thickness was particularly striking, since the number of oxygen molecules produced from the anode reaction depends solely on the operating current density. It could be hypothesized that the increase in gas thickness with increasing temperature was due to an increase in bubble size and detachment frequency in the anode channels, driven by the temperature dependent changes in fluid properties. Both the bubble size and detachment frequency can significantly affect the measured gas thickness since the gas thickness is measured over a prescribed time interval. Specifically, a larger-sized bubble travelling across the channel and a more frequent detachment frequency can manifest as a thicker layer of gas. The increase in gas thickness with increasing temperature may have also been influenced by additional factors, such as the decrease in surface tension and increased evaporation rate due to higher saturation pressure of liquid water.

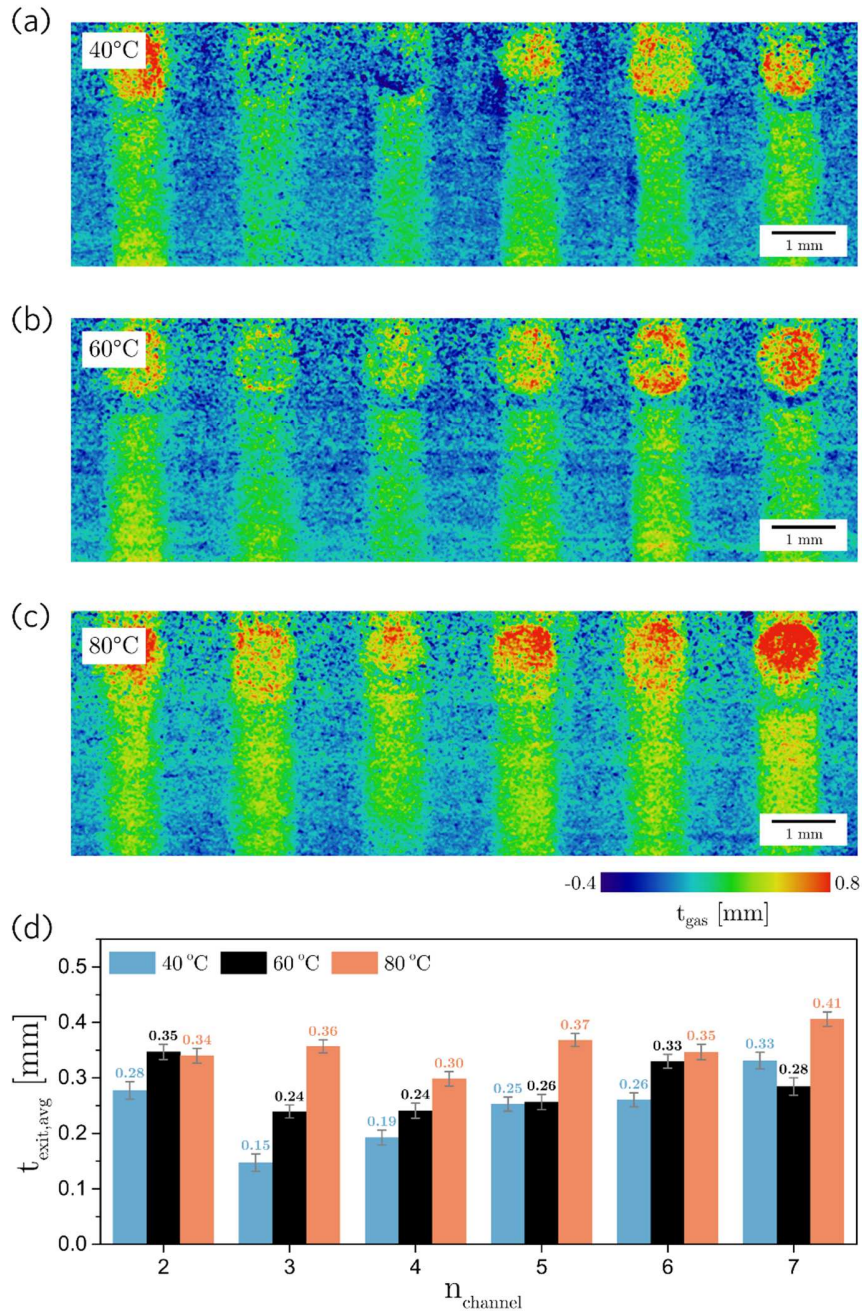


Figure 5: Processed images obtained from neutron radiographs during operating temperatures of 40 °C (a), 60 °C (b), and 80 °C (c) at an operating current density of 3.0 A/cm<sup>2</sup>; (d) Gas thicknesses in each channel shown in (a),(b), and (c). The error bars represent the 95 % confidence intervals. The mean exit gas thicknesses were 0.24 mm, 0.28 mm, and 0.35 mm for operating temperatures of 40 °C, 60 °C, and 80 °C, respectively. The error bars show 95 % confidence intervals based on the variation of thickness within each channel, and the value of the error bars was consistently  $\sim \pm 0.01$  mm. We observed an increase in gas thickness with increasing temperature in the majority of channels.

We initially expected that the larger quantity of gas present in the anode flow channel would impede liquid water transport and lead to an increased mass transport overpotential. Ito et al. [24] reported that when the gas significantly occupies the volume of the channel, the supply of reactant water becomes severely restricted. However, the electrochemical data showed, unexpectedly, that when the operating temperature increased from 40 °C to 80 °C, the mass transport overpotential decreased by 25 %, despite the 46 % increase in gas volume. Additional factors may have also contributed towards the reduced mass transport overpotential despite the increased gas thickness in the channels. For example, the decrease in surface tension may have led to a higher frequency of bubble detachment, subsequently promoting the coalescence of gas, as demonstrated by Li et al. [57,58] A higher frequency would manifest as a larger gas thickness observed via neutron images. Additionally, an increase in the gas volume in the channel due to a decrease in surface tension or increase in evaporation rate can lead to a transition from bubble flow to slug flow in the channels. This scenario has been previously observed via optical imaging and electrochemical impedance spectroscopy with an accompanying decrease in the mass transport overpotential [25]. Here, we propose that the effect of enhanced liquid water transport was attributed to the favorable changes in fluid properties (such as decrease in water viscosity), which contributed to the decrease in mass transport overpotential. Specifically, the decrease in water viscosity is relatively significant compared to changes in any other fluid property ( $6.53 \times 10^{-4}$  Pa (40 °C) and  $3.54 \times 10^{-4}$  Pa (80 °C) [49]), and we expect this change in viscosity to produce an enhanced liquid water flow distribution across the anode flow channels

We examined this hypothesis by comparing our analytical model results with the experimental results (Fig. 6). Specifically, the theoretical predictions of gas thickness as a function of current density were calculated based on the assumption that the liquid water delivery to each of the parallel flow channels was uniform, and we determined that the gas generation rate across the active area was also uniform by directly comparing the modelling results with the measured gas thickness via neutron imaging. We quantified the deviations between the theoretical and the experimental gas thicknesses by calculating the root-mean-square deviation (RMSD), which was 0.066 mm, 0.034 mm, and 0.025 mm for operating temperatures of 40 °C, 60 °C, and 80 °C, respectively. At the lowest operating temperature (40 °C), the mean quantity of gas exhibited relatively poor agreement with the theoretical curve (RMSD of 0.066 mm, Fig. 6a). This poor agreement suggested that the reactant delivery to the parallel flow channels and the gas generation rate were non-uniform. With a non-uniform water flow in each flow channel, the gas volume in each channel potentially varied significantly due to the varying rates of local gas generation [59,60]. Regions beneath water-starved channels do not have access to a sufficient supply of water, consequently manifesting as higher mass transport overpotentials [23].

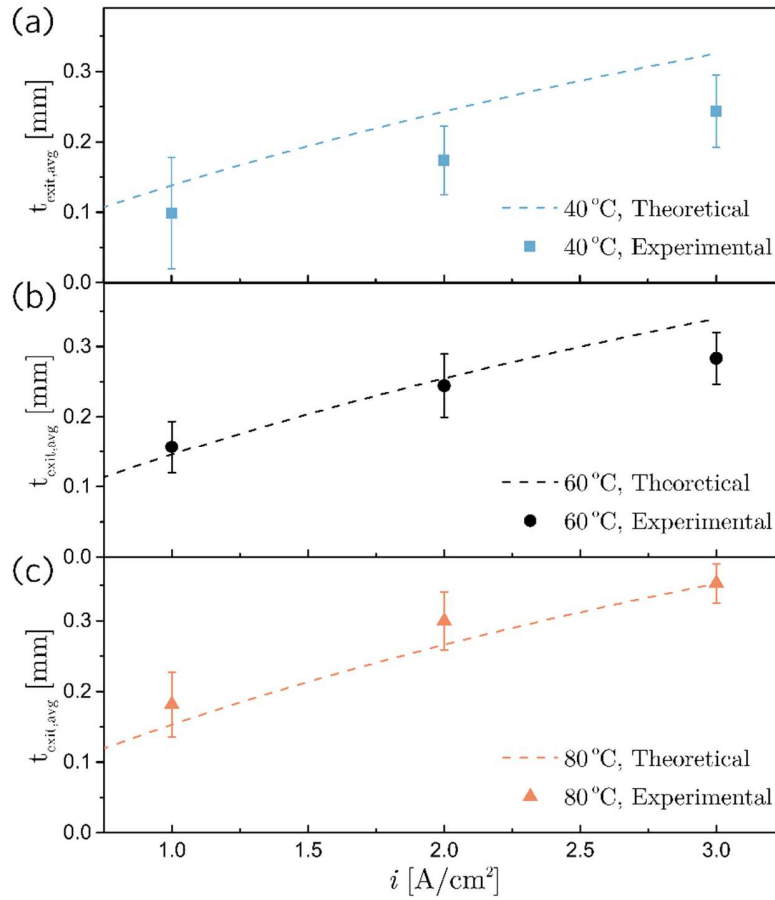


Figure 6: Mean exit gas thickness determined from *in operando* neutron radiography visualization at operating temperatures of (a) 40 °C, (b) 60 °C, and (c) 80 °C. The error bars represent the 95 % confidence intervals. The dashed lines indicate the theoretical exit gas thickness determined from the analytical model, assuming uniform liquid water distribution to each parallel flow channel and uniform current density operation. The root-mean-square deviations between the experimental and theoretical data are 0.066 mm, 0.034 mm, and 0.025 mm for 40 °C, 60 °C, and 80 °C, respectively. The theoretical and the experimental gas thicknesses at 80 °C exhibited the best agreement, whereas the theoretical and the experimental gas thicknesses at 40 °C exhibited the highest discrepancy, indicating a relatively uniform reactant delivery and local current density at higher temperature.

Under the highest operating temperature condition (80 °C), the mean quantity of gas showed good agreement with the theoretical curve (RMSD of 0.025 mm, Fig. 6c). This close agreement suggested that the reactant delivery to the parallel flow channels and the local current densities were uniform at 80 °C. This comparison between our theoretical and experimental gas thicknesses supports the hypothesis of enhanced liquid water transport leading to reduced mass

transport overpotential. Specifically, the enhanced uniformity in the liquid water distribution across the parallel flow channels is expected to suppress local increases in mass transport overpotential, subsequently lowering the overall mass transport overpotential. These results complement our previous findings on temperature-dependent two-phase flow near the PTL-CL interface [31]. Specifically, a higher temperature operation led to a more uniform distribution of gas near the PTL-CL interface, and this was most likely affected by the uniform distribution of liquid water across the anode flow channels presented here.

Under water starvation conditions (i.e. low stoichiometric ratio), the electrolyzer can experience high mass transport overpotentials [23,61]. In our work, we used a high overall stoichiometric ratio, thus water starvation was not expected. However, after comparing the experimental and numerical results, we propose that local variance in mass transport overpotential may exist due to the non-homogeneous distribution of liquid water in the parallel flow channels, which subsequently resulted in higher overall mass transport overpotentials at lower temperatures.

### *3.3 Two-Phase Pressure Drop Decreases with Increasing Temperature*

Thus far, we have demonstrated the advantages of higher operating temperature on the even distribution of liquid water to the parallel flow channels. In this section, we identified the mechanism of even liquid water distribution by calculating the two-phase pressure drop across the flow channel as a function of both current density and temperature with the Lockhart-Martinelli correlation. The pressure drop across the anode flow field is a key indicator for mass transport in PEM electrolyzers since permeation is one of the main mechanisms of liquid water transport [47].

As expected, we observed an increase in the two-phase pressure drop across the flow channels with increasing current density operation (Fig. 7a), which we attributed to the increasing product gas volume in the channel. In contrast, we observed a decrease in the two-phase pressure drop with increasing temperature. Surprisingly, the pressure drop decreased by 29 %, even though the mean gas thickness increased by 46 % when the operating temperature was increased from 40 °C to 80 °C at 3 A/cm<sup>2</sup>. This dramatic, temperature-dependent decrease in pressure drop illustrates that the fluid properties of the water dominate the two-phase pressure drop in comparison to the gas volume increase. Furthermore, the trends exhibited by the two-phase pressure drops (Fig. 7a) closely mirror the trends of mass transport overpotential (Fig. 3c), which justifies the two-phase pressure drop as a key parameter for characterizing two-phase flow in PEM electrolyzers.

It is important to note that the reported relationship between gas quantity in the anode flow channels and the mass transport overpotential is inconsistent in the literature [24-26, 30]. Here, we demonstrate that the effect of gas quantity in the flow channels on the mass transport overpotential can be characterized more consistently within the field of PEM electrolyzer research via determining the two-phase pressure drop. The two-phase pressure drop is affected by the gas quantity in the channels, as well as the operating conditions (i.e. temperature) and cell design (i.e. channel dimensions); this indicator will enable us to characterize the mass transport overpotential across varying operating conditions and cell designs.

Lower pressure drops were observed at higher operating temperatures, and the error bars were larger for  $T = 40\text{ }^{\circ}\text{C}$  relative to the error bars for  $T = 80\text{ }^{\circ}\text{C}$  (Fig. 7a). The average error bar values were  $\pm 1.69\text{ Pa}$ ,  $\pm 0.96\text{ Pa}$ , and  $\pm 0.87\text{ Pa}$  for  $T = 40\text{ }^{\circ}\text{C}$ ,  $60\text{ }^{\circ}\text{C}$ , and  $80\text{ }^{\circ}\text{C}$ , respectively. The larger error bar for  $T = 40\text{ }^{\circ}\text{C}$  is significant because it indicates the existence of large pressure differences between each channel, which would be accompanied by non-uniform distributions of liquid water. Liquid water is expected to flow preferentially in channels that exhibit lower pressure drops. In contrast to the results for  $T = 40\text{ }^{\circ}\text{C}$ , smaller error bars were observed at higher temperatures suggesting the presence of a more uniform distribution of liquid water across the parallel flow channels (as discussed in Section 3.2) due to a more uniform pressure drop across each channel (and lower overall pressure drop). This uniform distribution of liquid water is expected to prevent/suppress local increases in mass transport overpotential, consequently leading to lower overall mass transport overpotentials.

We performed a temperature-sensitivity analysis of the fluid properties involved in the two-phase pressure drop (seen in Fig. 7b). The calculated two-phase pressure drop was most sensitive to the water viscosity (decreased by 46 % when the temperature was increased from  $40\text{ }^{\circ}\text{C}$  to  $80\text{ }^{\circ}\text{C}$ ). Therefore, we attributed the experimentally observed decrease in mass transport overpotential with increasing temperature to the improved reactant delivery across the flow channels resulting from the decreasing water viscosity. Additionally, we observed that the two-phase pressure drops were relatively insensitive to gas density. The insensitivity to gas density suggests that the relative contribution of increasing gas content in the channels (driven by decreasing gas density) was insignificant relative to the relative contribution of enhanced water transport (driven by decreasing water viscosity). Furthermore, we observed a maximum decrease in pressure drop of

46 % (10.5 Pa) with decreasing water viscosity (as T increased from 40 °C to 80 °C) (Fig. 7b). In contrast, we observed a maximum increase in pressure drop of 23 % (3.1 Pa) with increasing current density from 1 A/cm<sup>2</sup> to 3 A/cm<sup>2</sup> (Fig. 6c). Therefore, the pressure drop was more significantly affected by the change in water viscosity than the change in gas content in the channels. Our combined observations from experiment and modelling demonstrated that increasing the operating temperature led to a decrease in mass transport overpotential, mainly due to enhanced homogeneity of water delivery across the anode flow channels (made possible by the decrease in water viscosity). Future work will include examining the effect of higher liquid water flow rates (> 20 mL/min) on the two-phase flow behaviour in the anode flow channels and the associated mass transport overpotential.

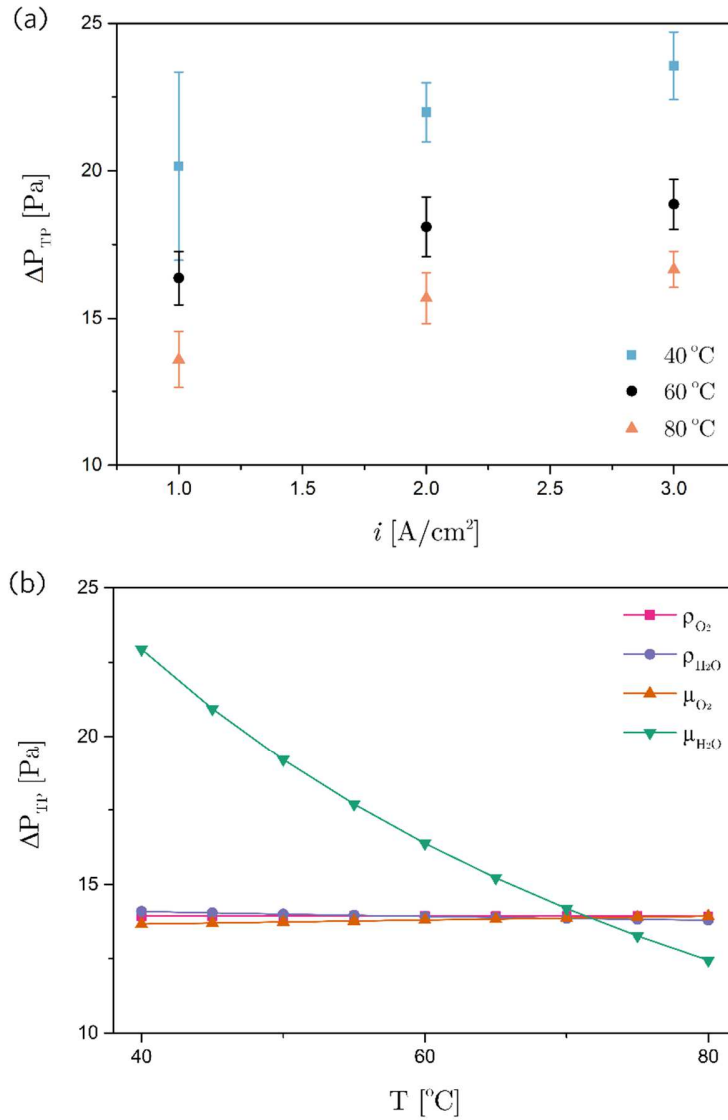


Figure 7: (a) Two-phase pressure drop across a single flow channel calculated using the Lockhart-Martinelli correlation. The error bars represent the 95 % confidence intervals. We observe a decrease in two-phase pressure drop with increasing temperature, a trend that closely resembles that of the mass transport overpotential (Fig. 3c); (b) Sensitivity analysis of the two-phase pressure drop and temperature-dependent fluid properties. During the sensitivity analysis the fixed variables were based on  $T = 80$  °C and  $i = 1.0$  A/cm<sup>2</sup>. We identified that the viscosity of water dominated the decrease in the two-phase pressure drop.

#### 4.0 Conclusion

In this work, we examined the effect of temperature on the multi-phase flow behaviour and the associated mass transport overpotential of LT-PEM electrolyzers. We used *in operando* neutron

radiography to visualize an electrolyzer designed in-house operating over a range of temperatures (40 °C, 60 °C, and 80 °C) and current densities (1.0 A/cm<sup>2</sup>, 2.0 A/cm<sup>2</sup>, and 3.0 A/cm<sup>2</sup>). We observed a 25 % decrease in the mass transport overpotential when we increased the temperature from 40 °C to 80 °C at 3.0 A/cm<sup>2</sup>. We attribute this decrease in mass transport overpotential to the more uniform delivery of liquid water to the catalyst layer, stemming from the enhanced two-phase flow behaviour in the flow channels. Despite this favourable and significant decrease in mass transport overpotential, our neutron radiographic visualization revealed a surprising 46 % increase in the quantity of gas with this temperature increase. To explain this counterintuitive result, we applied an analytical model of the gas channel and found that increasing the operating temperature encouraged a more uniform liquid water reactant distribution in the channel. We propose that the uniform distribution of liquid water to the parallel flow channels suppressed local increases in mass transport overpotential. Furthermore, we calculated the two-phase pressure drop across a single flow channel with the Lockhart-Martinelli correlation and found the pressure drop decreased by 29 % when the operating temperature increased from 40 °C to 80 °C. Even though we calculated an expected increase in the gas content with increasing current density, ultimately, the two-phase pressure drop exhibited a dominating decrease with increasing temperature. Furthermore, the two-phase pressure drop varied more significantly between the parallel channels at lower temperatures, and at these lower temperatures, we expected a higher local mass transport overpotential under channels which exhibited relatively high pressure drops. We performed a sensitivity analysis and found that the viscosity of water was the most influential fluid property affecting the pressure drop across the channel, thereby facilitating improved reactant delivery across the anode flow field. Our findings

support higher temperature operation, mainly owing to the decreased water viscosity enhancing the reactant delivery to the reaction sites.

In conclusion, we reconciled the effect of temperature on PEM electrolyzers – while increasing the temperature led to a higher content of gas in the channels, ultimately, the decrease in water viscosity dominated the temperature-dependent influence on LT-PEM electrolyzer performance through the enhanced homogeneity of reactant water delivery and the associated reduction in mass transport overpotential.

### **Acknowledgements**

Financial support from the Natural Sciences and Engineering Research Council of Canada (NSERC), the NSERC Collaborative Research and Training Experience Program (CREATE) in Distributed Generation for Remote Communities, and the Canada Research Chairs Program are gratefully acknowledged. Graduate scholarships to ChungHyuk Lee from the Bert Wasmund Graduate Fellowship in Sustainable Energy Research, Hatch Graduate Fellowship for Sustainable Energy Research, David Sanborn Scott Graduate Fellowship, and the Ontario Graduate Scholarship are gratefully acknowledged. NIST authors acknowledge support from the U.S. Department of Commerce, the NIST Radiation and Physics Division, the Director's office of NIST, and the NIST Center for Neutron Research.

## 6.0 Appendix

### *Appendix A: Detailed Calculation Procedure of the Two-Phase Pressure Drop*

Here, we detailed the calculation procedure used in this study for determining the two-phase pressure drop values. The procedure was adopted from Ito et al. [24] and was also employed by the work of Garcia-Navarro et al. [47]

Firstly, we determined the Reynolds number of the gaseous phase ( $Re_{\text{gas}}$ ), assuming the gas species is solely oxygen) and the liquid phase ( $Re_{\text{liq}}$ ) in the anode flow channel using the following equations.

$$Re_{\text{gas}} = \frac{G_{\text{H}_2\text{O},\text{in}} \cdot x \cdot t_{\text{channel}}}{\mu_{\text{O}_2}} \quad (\text{A.1})$$

$$Re_{\text{liq}} = \frac{G_{\text{H}_2\text{O},\text{in}} \cdot (1 - x) \cdot t_{\text{channel}}}{\mu_{\text{H}_2\text{O}}} \quad (\text{A.2})$$

When  $Re < 1000$ , the phase was considered laminar, and when  $Re > 2000$ , the phase was considered turbulent. Then, based on the type of flow, the frictional coefficient of liquid water was calculated to determine the pressure drop assuming liquid only in the anode flow channels ( $\Delta P_{\text{LO}}$ ):

$$C_f = \frac{56.9}{Re_{\text{H}_2\text{O}}} \text{ when } Re_{\text{liq}} < 1000 \quad (\text{A.3})$$

$$C_f = \frac{0.3164}{Re_{\text{H}_2\text{O}}^{0.25}} \text{ when } Re_{\text{liq}} > 2000 \quad (\text{A.4})$$

Then, based on the flow type of each phase, the corresponding equations for determining the Lockhart-Martinelli parameter (X) as well as the Chisholm parameter (C) (listed in Table 2) were

used. The Lockhart-Martinelli and Chisholm parameters were then substituted into Equation (13) to determine the two-phase multiplier ( $\phi_L^2$ ). Finally, the two-phase multiplier ( $\phi_L^2$ ) and the pressure drop assuming liquid phase only ( $\Delta P_{LO}$ ) were substituted into Equation (12) to determine the two-phase pressure drop ( $\Delta P_{TP}$ ).

#### *Appendix B: Sensitivity of the Analytical Model to the Water Content in the Membrane*

Here, we analyzed the sensitivity of our analytical model to the water content in the cathode side of the membrane. Diffusion was accounted for in this work since the cathode side of the electrolyzer was actively dried with dry nitrogen at 10 L/min. In the manuscript, the cathode side of the membrane was assumed to be completely dry (i.e.  $\lambda_{\text{cathode}} = 0$ ) to determine the water flux via diffusion across the membrane, since the cathode side was purged with dry nitrogen. However, due to electro-osmotic drag and diffusion, the true water content at the cathode side of the membrane is not expected to be zero in reality.

From our numerical modelling analysis, we identified that the water diffusion across the membrane (i.e.  $G_{\text{H}_2\text{O,diff}}$ ) had a negligible effect relative to the electro-osmotic drag of water across the membrane (i.e.  $G_{\text{H}_2\text{O,drag}}$ ) (Fig. A.1a). To justify this assumption, we first assumed a dry membrane at the cathode side and an operating temperature of 80 °C, whereby we observed that  $G_{\text{H}_2\text{O,drag}}$  was higher than  $G_{\text{H}_2\text{O,diff}}$  when  $i > 0.15 \text{ A/cm}^2$ . The assumption of a dry membrane at the cathode side may not always be physically representative, since the water content at the cathode side of the membrane should also depend on current density due to the presence of electro-osmotic drag. However, we assumed a dry membrane assumption to simulate the largest diffusion rate physically possible, since the rate of electro-osmotic drag increases with increasing

current density (thereby acting to decrease the rate of diffusion across the membrane). We further confirmed the negligible effect of diffusion by comparing the results of our model with the experimental observations of the cathode side of the membrane when completely dry and when completely wet (Fig A.1b). An average difference of only 0.03 % was found between the two experimental results, which highlights the negligible effect of diffusion.

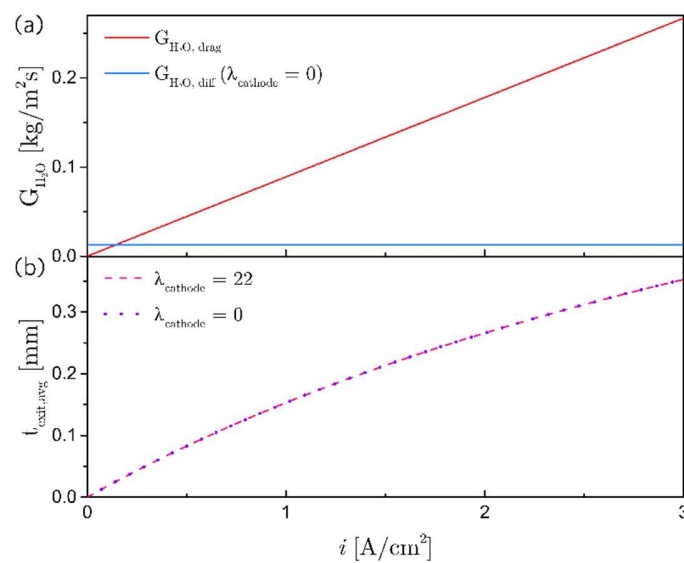


Fig A.1.: Sensitivity analysis of the effect of water diffusion across the membrane on the analytical model results. (a) Comparison of water flux due to electro-osmotic drag (red) and diffusion (blue). (b) Comparison of the analytical model results assuming the cathode side of the membrane is fully wet (pink-dashed) and fully dry (purple-dotted).

## 7.0 References

- [1] N. Armaroli, V. Balzani, ChemSusChem. 4 (2011) 21-36.
- [2] R. Kothari, D. Buddhi, R. Sawhney, Renewable and Sustainable Energy Reviews. 12 (2008) 553-563.
- [3] H. Wang, W. Li, T. Liu, X. Liu, X. Hu, Energy conversion and management. 183 (2019) 97-108.
- [4] O. Schmidt, A. Gambhir, I. Staffell, A. Hawkes, J. Nelson, S. Few, Int J Hydrogen Energy. 42 (2017) 30470-30492.

- [5] M. Kato, S. Maezawa, K. Sato, K. Oguro, *Appl. Energy*. 59 (1998) 261-271.
- [6] M. Carmo, D.L. Fritz, J. Mergel, D. Stolten, *Int J Hydrogen Energy*. 38 (2013) 4901-4934.
- [7] C.K. Mittelsteadt, *ECS Transactions*. 69 (2015) 205-211.
- [8] C. Wang, F. Lan, Z. He, X. Xie, Y. Zhao, H. Hou, L. Guo, V. Murugadoss, H. Liu, Q. Shao, *ChemSusChem*. 12 (2019) 1576-1590.
- [9] J.W.D. Ng, T.R. Hellstern, J. Kibsgaard, A.C. Hinckley, J.D. Benck, T.F. Jaramillo, *ChemSusChem*. 8 (2015) 3512-3519.
- [10] G. Yang, S. Yu, Z. Kang, Y. Dohrmann, G. Bender, B.S. Pivovar, J.B. Green Jr, S.T. Retterer, D.A. Cullen, F. Zhang, *Energy conversion and management*. 182 (2019) 108-116.
- [11] P. Lettenmeier, R. Wang, R. Abouatallah, B. Saruhan, O. Freitag, P. Gazdzicki, T. Morawietz, R. Hiesgen, A. Gago, K. Friedrich, *Scientific Reports*. 7 (2017) 1-12.
- [12] U. Babic, M. Suermann, F.N. Büchi, L. Gubler, T.J. Schmidt, *J. Electrochem. Soc.* 164 (2017) F387-F399.
- [13] C.H. Lee, R. Banerjee, F. Arbabi, J. Hinebaugh, A. Bazylak, (2016) V001T07A003.
- [14] M. Suermann, T.J. Schmidt, F.N. Büchi, *ECS Transactions*. 69 (2015) 1141-1148.
- [15] U. Babic, T.J. Schmidt, L. Gubler, *J. Electrochem. Soc.* 165 (2018) J3016-J3018.
- [16] P. Trinke, G. Keeley, M. Carmo, B. Benschmann, R. Hanke-Rauschenbach, *J. Electrochem. Soc.* 166 (2019) F465-F471.
- [17] H. Li, A. Inada, T. Fujigaya, H. Nakajima, K. Sasaki, K. Ito, *Journal of Power Sources*. 318 (2016) 192-199.
- [18] S. Grigoriev, P. Millet, S. Volobuev, V. Fateev, *Int J Hydrogen Energy*. 34 (2009) 4968-4973.
- [19] J. Mo, Z. Kang, G. Yang, S.T. Retterer, D.A. Cullen, T.J. Toops, J.B. Green, F.-. Zhang, *Appl. Energy*. 177 (2016) 817-822.
- [20] Z. Kang, J. Mo, G. Yang, Y. Li, D.A. Talley, S.T. Retterer, D.A. Cullen, T.J. Toops, M.P. Brady, G. Bender, *Appl. Energy*. 206 (2017) 983-990.
- [21] E.T. Ojong, J.T.H. Kwan, A. Nouri-Khorasani, A. Bonakdarpour, D.P. Wilkinson, T. Smolinka, *Int J Hydrogen Energy*. 42 (2017) 25831-25847.
- [22] M. Suermann, T.J. Schmidt, F.N. Büchi, *Electrochim. Acta*. 211 (2016) 989-997.

- [23] S. Sun, Y. Xiao, D. Liang, Z. Shao, H. Yu, M. Hou, B. Yi, *RSC Advances*. 5 (2015) 14506-14513.
- [24] H. Ito, T. Maeda, A. Nakano, Y. Hasegawa, N. Yokoi, C.M. Hwang, M. Ishida, A. Kato, T. Yoshida, *Int J Hydrogen Energy*. 35 (2010) 9550-9560.
- [25] I. Dedigama, P. Angeli, K. Ayers, J.B. Robinson, P.R. Shearing, D. Tsaoulidis, D.J. Brett, *Int J Hydrogen Energy*. 39 (2014) 4468-4482.
- [26] I. Dedigama, P. Angeli, N. Dijk, J. Millichamp, D. Tsaoulidis, P.R. Shearing, D.J.L. Brett, *J. Power Sources*. 265 (2014) 97-103.
- [27] F. Aubras, J. Deseure, J. Kadjo, I. Dedigama, J. Majasan, B. Grondin-Perez, J. Chabriat, D. Brett, *Int J Hydrogen Energy*. 42 (2017) 26203-26216.
- [28] J.O. Majasan, J.I. Cho, I. Dedigama, D. Tsaoulidis, P. Shearing, D.J. Brett, *Int J Hydrogen Energy*. 43 (2018) 15659-15672.
- [29] Y. Li, G. Yang, S. Yu, Z. Kang, D.A. Talley, F. Zhang, *Energy Conversion and Management*. 199 (2019) 111935.
- [30] A. Zinser, G. Papakonstantinou, K. Sundmacher, *Int J Hydrogen Energy*. (2019).
- [31] C. Lee, J.K. Lee, B. Zhao, K.F. Fahy, J.M. LaManna, E. Baltic, D.S. Hussey, D.L. Jacobson, V.P. Schulz, A. Bazylak, *Journal of Power Sources*. 446 (2020) 227312.
- [32] O.F. Selamet, U. Pasaogullari, D.S. Hussey, D.L. Jacobson, M.D. Mat, *Int. J. Hydrogen Energy*. 38 (2013) 5823-5835.
- [33] M.A. Hoeh, T. Arlt, N. Kardjilov, I. Manke, J. Banhart, D.L. Fritz, J. Ehlert, D.L. Fritz, W. Lüke, W. Lehnert, *ECS Transactions*. 69 (2015) 1135-1140.
- [34] M.A. Hoeh, T. Arlt, I. Manke, J. Banhart, D.L. Fritz, W. Maier, W. Lehnert, *Electrochemistry Communications*. 55 (2015) 55-59.
- [35] E. Leonard, A.D. Shum, S. Normile, D.C. Sabarirajan, D.G. Yared, X. Xiao, I.V. Zenyuk, *Electrochim.Acta*. 276 (2018) 424-433.
- [36] O.F. Selamet, P. Deevanhxay, S. Tsushima, S. Hirai, *Journal of Power Sources*. 296 (2015) 133-141.
- [37] J. Seweryn, J. Biesdorf, T.J. Schmidt, P. Boillat, *J.Electrochem.Soc*. 163 (2016) F3009-F3011.
- [38] C. Lee, R. Banerjee, N. Ge, J.K. Lee, B. Zhao, E. Baltic, J.M. LaManna, D.S. Hussey, D.L. Jacobson, R. Abouatallah, R. Wang, A. Bazylak, *Electrochimica Acta*. 279 (2018) 91-98.

- [39] O. Panchenko, E. Borgardt, W. Zwaygardt, F.J. Hackemüller, M. Bram, N. Kardjilov, T. Arlt, I. Manke, M. Müller, D. Stolten, *J.Power Sources*. 390 (2018) 108-115.
- [40] O. Panchenko, L. Giesenberg, E. Borgardt, W. Zwaygardt, N. Kardjilov, H. Markötter, T. Arlt, I. Manke, M. Müller, D. Stolten, *Energies*. 12 (2019) 350.
- [41] F. De Beer, J. Van der Merwe, D. Bessarabov, *Physics Procedia*. 88 (2017) 19-26.
- [42] R.L. LeRoy, C.T. Bowen, D.J. LeRoy, *J.Electrochem.Soc.* 127 (1980) 1954-1962.
- [43] B. Münch, P. Trtik, F. Marone, M. Stampanoni, *Optics Express*. 17 (2009) 8567-8591.
- [44] D.S. Hussey, D. Spornjak, A.Z. Weber, R. Mukundan, J. Fairweather, E.L. Brosha, J. Davey, J.S. Spendelow, D.L. Jacobson, R.L. Borup, *J.Appl.Phys.* 112 (2012) 104906.
- [45] S. Motupally, A.J. Becker, J.W. Weidner, *J.Electrochem.Soc.* 147 (2000) 3171-3177.
- [46] R. Banerjee, D. Howe, V. Mejjia, S.G. Kandlikar, *International Journal of Hydrogen Energy*. 39 (2014) 17791-17801.
- [47] J. Garcia-Navarro, M. Schulze, K.A. Friedrich, *ACS Sustainable Chemistry & Engineering*. 7 (2018) 1600-1610.
- [48] R. Lockhart, R. Martinelli, *Chem.Eng.Prog.* 45 (1949) 39-48.
- [49] E.W. Lemmon, M.O. McLinden, D.G. Friend (Eds), *Thermophysical properties of fluid systems*, National Institute of Standards and Technology, Gaithersburg MD, 1998.
- [50] N. Vargaftik, B. Volkov, L. Voljak, *Journal of Physical and Chemical Reference Data*. 12 (1983) 817-820.
- [51] H. Ito, T. Maeda, A. Nakano, A. Kato, T. Yoshida, *Electrochim.Acta*. 100 (2013) 242-248.
- [52] R.W. Kopitzke, C.A. Linkous, H.R. Anderson, G.L. Nelson, *J.Electrochem.Soc.* 147 (2000) 1677-1681.
- [53] P. Trinke, G. Keeley, M. Carmo, B. Benschmann, R. Hanke-Rauschenbach, *J.Electrochem.Soc.* 166 (2019) F465-F471.
- [54] T. Schuler, T.J. Schmidt, F.N. Büchi, *J.Electrochem.Soc.* 166 (2019) F555-F565.
- [55] U. Babic, E. Nilsson, A. Pătru, T.J. Schmidt, L. Gubler, *J.Electrochem.Soc.* 166 (2019) F214-F220.
- [56] Ö.F. Selamet, M.C. Acar, M.D. Mat, Y. Kaplan, *Int.J.Energy Res.* 37 (2013) 457-467.

[57] Y. Li, Z. Kang, J. Mo, G. Yang, S. Yu, D.A. Talley, B. Han, F. Zhang, *Int J Hydrogen Energy*. 43 (2018) 11223-11233.

[58] Y. Li, Z. Kang, X. Deng, G. Yang, S. Yu, J. Mo, D.A. Talley, G.K. Jennings, F. Zhang, *Electrochim.Acta*. 298 (2019) 704-708.

[59] J. Nie, Y. Chen, S. Cohen, B.D. Carter, R.F. Boehm, *International Journal of Thermal Sciences*. 48 (2009) 1914-1922.

[60] J. Nie, Y. Chen, *Int J Hydrogen Energy*. 35 (2010) 3183-3197.

[61] C. Immerz, B. Bensmann, P. Trinke, M. Suermann, R. Hanke-Rauschenbach, *J.Electrochem.Soc*. 165 (2018) F1292-F1299.

